DOI: 10.1002/ejic.200800956

Corundum-Type In_2O_3 Urchin-Like Nanostructures: Synthesis Derived from Orthorhombic InOOH and Application in Photocatalysis

Li-Yong Chen,[a] Yi Liang,[a] and Zu-De Zhang*[a]

Keywords: Nanostructures / Indium / Photochemistry / Hydrolysis

A facile route was applied to synthesize indium oxyhydroxide (InOOH) with urchin-like nanostructures through polymer-assisted hydrolysis of the In^{3+} cation in water/ethanol mixed solvent. The uniform InOOH urchin-like nanostructures are composed of nanorods with a diameter of several nanometers and a length up to 100 nm. Investigation of the effects of various reaction parameters reveals that poly(ethylene glycol)-1000 (PEG-1000) and reaction temperature have significant influences on the morphology of the as-prepared products. The formation of InOOH urchin-like nanostructures can be due to anisotropic structure and PEG-1000 selective adsorption. By annealing the preobtained InOOH precursor at 500 °C under ambient pressure, metastable hexagonal indium oxide (H-In_2O_3) urchin-like nanostructures, inheriting the morphology of its precursor in the transformation process, were obtained. The photocatalytic activity of as-prepared H-In_2O_3 was evaluated by photodegradation of rhodamine B (RhB) dye under ultraviolet (UV) light illumination. The stability of the photocatalytic performance of H-In_2O_3 urchin-like nanostructures was investigated by circulating run tests in the photodegradation of RhB.

Introduction

Recently, much effort has been devoted to the morphological control of metal-based semiconductor nanomaterials owing to their unique physical and chemical properties.[1] As one of the most important metal-based semiconductors, indium oxide (In_2O_3) with a direct bandgap of 3.55–3.75 eV has been widely used in optoelectronic devices such as solar cells, flat-panel displays, gas sensors, and photocatalysis.[2] Usually, In_2O_3 prefers to crystallize in a cubic bixbyite-type structure (C-In_2O_3) under normal conditions. To meet different requirements, C-In_2O_3 with different morphologies, including nanoparticles, nanowires, nanobelts, nanocrystal chains, pyramid-like crystals, nanotubes, and three-dimensional (3D) structures,[3] has been synthesized. More recently, the hexagonal corundum-type In_2O_3 (H-In_2O_3), a high-pressure modification, has become particularly attractive because the metastable phase is a route toward creating new materials.[4] Some notable works have appeared for the preparation of metastable H-In_2O_3 under ambient pressure.[5]

Of these synthesis strategies, a general route to prepare In_2O_3 is by thermal treatment of its precursors: indium hydroxide or oxyhydroxide. In_2O_3 with various desired morphologies has been synthesized by controlling the morphologies of its precursors, because In_2O_3 can inherit their morphologies during the calcination process. However, the fabrication of well-defined H-In_2O_3 with complex 3D structures is usually difficult, because control of the nucleation and growth of nanomaterials is still a challenge.[6] Thus, it is important to develop innovative and convenient techniques for fabricating H-In_2O_3 nanomaterials with 3D structures under mild conditions and at low cost. Herein, our research teams provide a simple, controllable route to achieve the desired H-In_2O_3 with uniform morphology through annealing the InOOH precursor at 500 °C and under ambient pressure. The InOOH precursor with urchin-like nanostructures can be prepared through polymer-assisted hydrolysis of the In^{3+} cation in water/ethanol mixed solvent. On the basis of this strategy, the as-obtained H-In_2O_3 may well inherit the morphology of its precursor and can also exhibit urchin-like nanostructures.

The urchin-like H-In_2O_3 nanostructures may be expected to find potential application in photocatalysis, because a well-defined morphology and crystal structure have been regarded as critical factors that may show evidence for some novel and unexpected properties. Photocatalysis of some semiconductors as photocatalysts is widely considered as an emerging technology for solving environmental problems, in particular, for the removal of organic contaminants.[7] As an important wide bandgap semiconductor, In_2O_3 has been applied to improve the photocatalytic efficiency of other semiconductors and has also been used as a photocatalyst alone.[8] In this paper, for the first time we report the photo-

[a] Department of Chemistry, University of Science and Technology of China,
Hefei, Anhui 230026, P. R. China
Fax: +86-551-3601592
E-mail: zzd@ustc.edu.cn

Supporting information for this article is available on the WWW under http://www.eurjic.org or from the author.

catalysis of H-In_2O_3 with urchin-like nanostructures. The photodegradation of rhodamine B (RhB) was employed to evaluate the photocatalytic activities of H-In_2O_3 under ultraviolet (UV) light illumination.

Results and Discussion

Phase and Purity of the Samples

X-ray diffraction was used to verify the crystal structures and the phase purities of the samples. A typical XRD pattern of the white products prepared by the solvothermal method at 140 °C for 16 h is shown in Figure 1a, where the reflection peaks can be indexed to orthorhombic InOOH (JCPDS card 17–0549, a = 5.26 Å, b = 4.56 Å, c = 3.27 Å). There are no characteristic peaks of $In(OH)_3$ observed. However, the identity of the first reflection peak at 2θ = 20.5° cannot be established on the basis of available literature. A similar diffraction peak was observed in a previous report.[5e] The relatively small size of the crystallites of the product makes the diffraction peaks much broader than that of the corresponding standard pattern. Additionally, (002) plane reflection appears less broad than the others in the XRD, indicating that the samples could tend to be preferentially oriented along [001] direction.

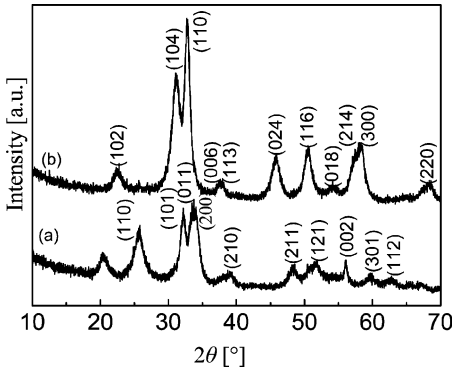

Figure 1. XRD patterns of the precursor (a) before and (b) after annealing at 500 °C for 5 min under ambient pressure.

Figure 1b is the corresponding XRD patterns of the pale-yellow samples obtained by annealing the InOOH precursor at 500 °C for 5 min. The reflection peaks in the XRD patterns can be ascribed to pure H-In_2O_3 (JCPDS card 22–0336, a = 5.49 Å, c = 14.52 Å) and no other impurities peaks are observed, indicating that the precursor was completely transformed into H-In_2O_3 under the annealing conditions. The broad diffraction peaks indicate that the products tend to be small in size.

The XPS survey spectrum of the as-prepared H-In_2O_3 materials (Figure S1a) reveals that the sample is composed of two elements: indium and oxygen. The two strong peaks at 444.3 and 451.9 eV (Figure S1b) can be attributed to binding energies of In $3d_{5/3}$ and In $3d_{3/2}$, respectively.[9] The peaks at 530.0 and 531.7 eV (Figure S1c) can be assigned to the binding energy of the O 1s transition. However, the peak at 531.7 eV is due to absorption of O_2 impurities on the surface of the sample, as urchin-like nanostructure materials exhibit a high surface-to-volume ratio.[10] According to the peak areas of In $3d_{5/3}$ and O 1s (530.0 eV), The atomic ratio of In to O is about 1:1.23, which can be attributed to oxygen vacancies formed during the calcination process.

The Morphology of the As-Obtained Samples

The size and typical morphologies of both the InOOH and In_2O_3 samples were illustrated by FE-SEM and TEM images. The panoramic FE-SEM image of InOOH is shown in Figure 2a, indicating that the InOOH products consist of large quantities of uniform urchin-like nanostructures with a diameter of 1–2 μm. Interestingly, through careful observation of the magnified FE-SEM images of InOOH (Figure 2b and 2c), it can be found that the surface of the urchin-like nanostructures is assembled by nanorods with a diameter of several nanometers and a length up to 100 nm. The TEM images of InOOH are shown in Figure 2d and 2e, which further reveal that the InOOH precursor has urchin-like nanostructures. A magnified TEM image of InOOH (Figure 2e) indicates that the nanorods on the surfaces have a very small diameter and also narrow size distribution. More details about the InOOH nanorod microstructures are investigated by the selected area electron diffraction (SAED) and HRTEM. There are several diffraction rings in the ED pattern (Figure 2e, inset). A relatively strong diffraction ring can be indexed to the (101) plane reflection of the orthorhombic InOOH. The HRTEM image, taken from a randomly chosen nanorod, exhibits lattice planes with spacing of 0.279 and 0.265 nm (Figure 2f), corresponding to the d spacing of the (101) and (200) planes of orthorhombic InOOH, respectively. The angle between the (101) and (200) planes was calculated to be 58.3°, which is in accordance with the interplanar angle of lattice fringes

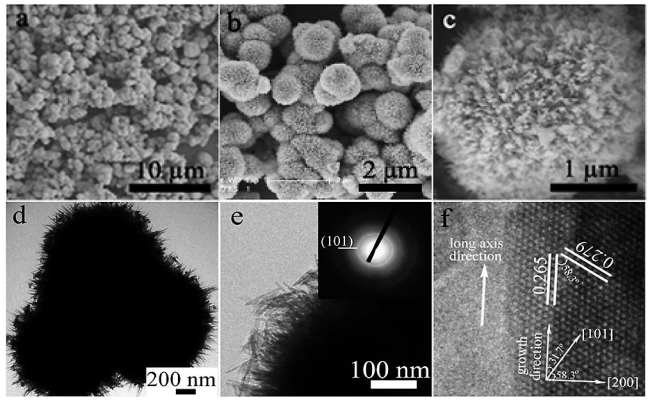

Figure 2. FESEM images of the InOOH precursor with urchin-like structures prepared at 140 °C: (a) panoramic morphologies, (b) low-magnification, and (c) high-magnification images. TEM images of the InOOH urchin-like nanostructures: (d) low-magnification and (e) high-magnification images. (f) HRTEM image of an InOOH nanorod. [The inset of (e) is the corresponding ED pattern of the as-obtained InOOH].

by measure. From the HRTEM image, the [200] direction is perpendicular to the growth direction of the nanorods. According to Equation (1), only the (002) and (031) planes are perpendicular to the (200) plane. However, the angle between the (031) and (101) planes was calculated to be 43.8°, and the calculated angle of 31.8° between (002) and (101) is close to the measured angle of 31.7° between the growth direction and the (101) lattice fringes. Hence, the [001] direction can be the growth direction of the InOOH nanorods, which is in agreement with the XRD analytical result. The HRTEM image indicates that these nanorods are single-crystalline InOOH.

$$\cos\phi = \frac{\frac{h_1h_2}{a^2} + \frac{k_1k_2}{b^2} + \frac{l_1l_2}{c^2}}{\sqrt{(\frac{h_1^2}{a^2} + \frac{k_1^2}{b^2} + \frac{l_1^2}{c^2})(\frac{h_2^2}{a^2} + \frac{k_2^2}{b^2} + \frac{l_2^2}{c^2})}} \quad (1)$$

FESEM and TEM images, as shown in Figure 3a–e, provide direct information about the size and morphology of the final H-In_2O_3 products, which suggests that H-In_2O_3 inherits the urchin-like structures from its InOOH precursor. The H-In_2O_3 urchin-like structures have diameters ranging from 1 to 2 μm, and the nanorods on the surfaces have a length of about 100 nm. The SAED pattern of the H-In_2O_3 urchin-like nanostructures is shown in the inset of Figure 3e. The first and the second diffraction rings in the SAED pattern correspond to (104) and (214) of H-In_2O_3, respectively. An HRTEM image of a single H-In_2O_3 nanorod is shown in Figure 3f, where the spacing of the lattice fringes was measured to be 0.285 nm, consistent with the (104) interplanar distance of H-In_2O_3, indicating that nanorods have a single-crystalline nature.

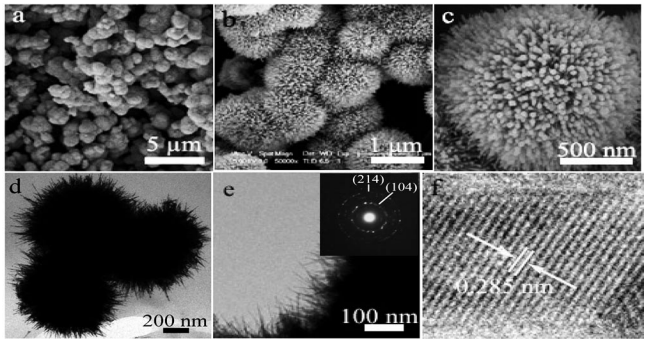

Figure 3. FESEM images of the H-In_2O_3 urchin-like structures by annealing the precursor at 500 °C for 5 min under ambient pressure: (a) panoramic morphologies, (b) low-magnification, and (c) high-magnification images. TEM images of the as-obtained H-In_2O_3 urchin-like nanostructures: (d) low-magnification and (e) high-magnification images. (f) HRTEM image of an H-In_2O_3 nanorod. [The inset of (e) is the corresponding ED pattern of the as-obtained H-In_2O_3].

Formation Mechanism of InOOH Urchin-Like Nanostructures

In this experiment, a two-step fabrication strategy was employed: firstly, the InOOH precursor with urchin-like nanostructures was prepared by a simple mixed solvothermal route in ethanol/water binary system; then, metastable H-In_2O_3 nanostructures were obtained under ambient pressure by the thermal decomposition of the InOOH precursor at 500 °C. The chemical reactions depicted in Equations (2), (3), (4), and (5) occurred in the formation of the H-In_2O_3 product.

$$CO(NH_2)_2 + H_2O \rightarrow CO_2 + 2NH_3 \quad (2)$$

$$In^{3+} + 3NH_3 + 3H_2O \rightarrow In(OH)_3 + 3NH_4^+ \quad (3)$$

$$In(OH)_3 \rightarrow InOOH + H_2O \quad (4)$$

$$2InOOH \rightarrow H\text{-}In_2O_3 + H_2O \quad (5)$$

The conversion from InOOH into H-In_2O_3 during the calcinations in air was studied by TG/DTA, as shown in Figure S2. The TGA curve of InOOH suggests that weight loss occurs in the temperature range from 50 to 550 °C. The loss weight between 50 and 300 °C originates from evaporation of the physically adsorbed water on the surface of InOOH and the DTA curve shows an exothermic process during this temperature range. The other weight loss is around 6.5% in the temperature range from 300 to 550 °C, which is very close to the amount of H_2O produced by the complete decomposition of InOOH [Equation (5)]. Also, another exothermic peak around 300 °C is presented in this DTA curve, which suggests it could be the onset of dehydration of InOOH. Additionally, there is another endothermal peak at 240 °C in the DTA curve, which may be related to the decomposition of the residual amount of poly(ethylene glycol)-1000 (PEG-1000) on the surface of InOOH.

In order to understand the formation of InOOH urchin-like nanostructures, we studied the influence of different parameters on the shape of products systematically. Some controlled experiments with different amounts of PEG-1000 were carried out. The obtained samples consisted of an uneven spherical aggregation of nanoparticles with a few nanorods on its surface (Figure 4a) when PEG-1000 is not added into the present system. When PEG-1000 (0.1 g) was introduced into the synthesis system, the morphology of the sample presents quasi-urchin-like nanostructures (Figure 4b). These experimental results reveal that PEG-1000 is favorable for the formation of InOOH nanorods, which can be attributed to PEG-1000 as capping agent that selectively adsorbs at different crystallographic facets of the growing crystals to achieve anisotropic crystal growth kinetically. Also, it was found that the reaction temperature had an influence on the morphology of prepared InOOH. Figure 4c shows the TEM image of products prepared at a reaction temperature of 160 °C in the presence of PEG-1000 (0.1 g). Nanostructures with hollow interiors were obtained, which is confirmed by the contrast between the dark edges and the pale centers. The formation of hollow structures assembled with nanoparticles is attributed to the large amount of microbubbles of CO_2 generated from the hydrolysis of urea at a relatively high reaction temperature, which serve as the aggregation center.[11] Driven by the minimiz-

ation of interfacial energy, small InOOH nanocrystals may aggregate around the gas–liquid interface between CO_2 and solution and finally hollow InOOH nanostructures form. Moreover, the InOOH nanocrystals do not grow into an anisotropic structure, because the interaction between the PEG-1000 molecule and the surface of the particles is weaker at high temperature than at low temperature, which affects the absorption of the polymer on the surface of the particles at 160 °C.

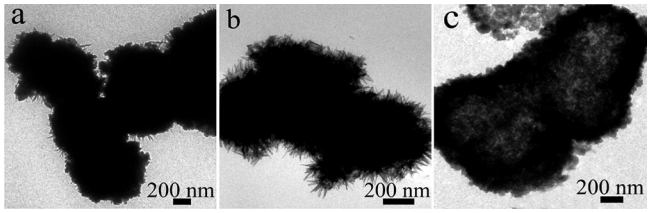

Figure 4. TEM images of InOOH prepared under different reaction conditions: (a) 140 °C and $m_{PEG-1000} = 0$, (b) 140 °C and $m_{PEG-1000} = 0.1$ g, and (c) 160 °C and $m_{PEG-1000} = 0.1$ g.

Additionally, to shed light on the formation of InOOH urchin-like nanostructures in detail, time-dependent experiments involved in their growth process at various stages were followed by TEM and XRD. Figure 5 reveals the variation of the morphology and phase of the samples, which were prepared at various reaction stages. The TEM image of a sample obtained after 1 h (Figure 5a) shows that particles, covered by a polymer and corresponding to lighter shaded area, are formed. The TEM image of the sample by solvothermal treatment for 2 h, as shown in Figure 5b, reveals that many particles with a relatively large size are formed. When the reaction time was prolonged to 2.5 h, some initial rod-like structures were formed on the surface of the agglomerates (Figure 5c). XRD analyses (Figure 5f, curves 1–3) identify them as poorly crystallized InOOH. With a prolonged solvothermal treatment time, rudiment urchin-like structures were obtained (Figure 5d). The XRD pattern (Figure 5f, curve 4) confirms that the samples are well-crystallized InOOH. For better comparison, the TEM image and XRD pattern of the desired InOOH are also shown in Figure 5e and 5f (curve 5), respectively. On the basis of Equation (3), the $In(OH)_3$ phase should be obtained during the growth process. However, from these XRD patterns, the characteristic peaks of $In(OH)_3$ are not found. In comparison to the experiments in the water/ethanol mixed solvent, this experiment was performed in pure water instead of the mixture and the cubic phase $In(OH)_3$ was obtained, which can be attributed to the hydrolysis of In^{3+} [Equation (3)]. Hence, the fact that $In(OH)_3$ instantly dehydrolyzes to form InOOH as soon as $In(OH)_3$ forms could be the reason that the characteristic peaks of $In(OH)_3$ are not found in the XRD patterns. Experiments with different reaction time were also monitored by FTIR (Figure S3). Although most assignments are straightforward, some vibration peaks are different from pure PEG-1000. The variation can be explained by PEG-1000 as capping agent molecules existing in the products and adsorbing on the surface of the products, which is in agreement with the results of TGA.

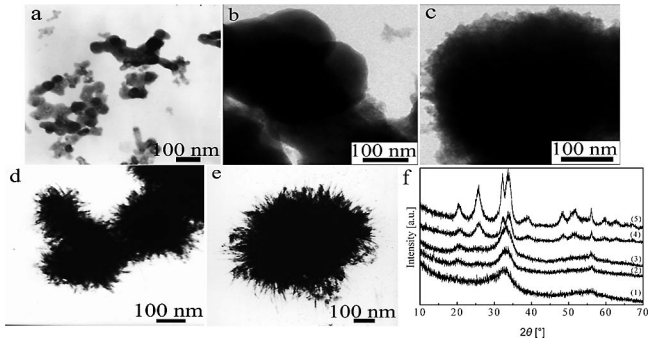

Figure 5. TEM images of precipitate at 140 °C with different reaction times: (a) 1 h, (b) 2 h, (c) 2.5 h (d) 4 h, and (e) 16 h. (f) Curves 1–5 correspond to the XRD patterns of samples from 1 to 16 h.

On the basis of the above information, the polymer-assisted anisotropic growth mechanism for the InOOH urchin-like nanostructures could be rationally supported. At an early stage of reaction, the poorly crystallized nanoparticles are formed owing to the kinetically driven hydrolysis of In^{3+},[12] and the PEG-1000 additive is absorbed on the particles surface. With extending the solvothermal treatment time, because the solute is transported from the solution to the crystal interface, it becomes incorporated into the crystal by surface kinetics, and the nanoparticles with a big size are formed. Owing to anisotropic crystal structure and PEG-1000 molecules, which selectively adsorb onto the lateral surfaces of InOOH nanocrystals, InOOH nanocrystals preferentially grow along the [001] direction and initial rod-like structures are yielded on the edge of the particles.[13] When the reaction time is further prolonged, the rod-like structures grow longer and these nanorods are assembled into the InOOH urchin-like structures to reduce the interfacial energy of small nanocrystals.

Photocatalysis Properties

The photocatalytic behavior of semiconductors is mainly dependent on the separation of photogenerated electron-hole pairs[14] and transfer the separated electrons from photocatalyst to the organic pollutants through the oxygen vacancy defects on the surface of photocatalyst.[15] In this paper, oxygen vacancy defects on the surface of H-In_2O_3 nanomaterials are generated due to heat treatment, which can be proved by the XPS spectrum. RhB is one kind of organic dye and often used as a model pollutant to study the photocatalytic activity or performance of nanomaterials. The maximal absorbance of RhB is at ca. 543 nm.

Figure 6a shows the UV/Vis adsorption spectra of an RhB ethanol solution in the presence of H-In_2O_3 urchin-like nanomaterials under UV light irradiation for various durations. The absorption peaks corresponding to RhB at 543 nm gradually decrease with prolonged irradiation times.

During this process, the pink color of the RhB solution gradually fades with increasingly longer irradiation time. These results indicate that RhB obviously undergoes degradation under the catalysis of H-In_2O_3 urchin-like nanostructures. Figure 6b shows the efficiencies of the photocatalytic degradation under UV light irradiation. The photodegradation efficiency is defined as the ratio between the absorbance C of RhB solution at the maximal absorption peaks with different irradiation time and the absorbance C_0 of the starting RhB solution before irradiation. Blank tests without any catalyst (Figure 6b, curve 1) under UV light exhibit little photolysis. The photodegradation efficiency is ca. 19% after 3 h, which demonstrates that the degradation of RhB is extremely slow without a photocatalyst under UV light illumination. However, as indicated in curves 2 and 3 of Figure 6b, the concentration of RhB obviously decreases with each of the In_2O_3 samples as a photocatalyst under exposure to UV light, revealing the obvious photocatalytic ability of In_2O_3. The photodegradation efficiency is 69 and 86%, corresponding to In_2O_3 nanocubes[16] and In_2O_3 urchin-like nanostructures, respectively, when the RhB/In_2O_3 suspension is irradiated for 3 h. These experimental results reveal that In_2O_3 urchin-like nanostructures have superior photocatalytic activity over In_2O_3 nanocubes, which can be attributed to the special structures of urchin-like In_2O_3, size effects of the nanorods, and a large surface area. Compared with nanocubes, urchin-like nanostructures can maintain a high active surface area even in aggregation due to the hierarchical structure, which is called the structure-induced enhancement of the photocatalytic performance,[17] and, the small size of the nanorods can reduce the recombination opportunities of the electron-hole pairs that could effectively move to the surface to degrade RhB, which improves photocatalysis performance.[18] Moreover, BET measurements show that the specific surface area of H-In_2O_3 urchin-like nanostructures is 30 $m^2 g^{-1}$, whereas that of In_2O_3 nanocubes is 21 $m^2 g^{-1}$. Hence, the relatively high photocatalytic efficiency of H-In_2O_3 can also be attributed to its large surface area, which is beneficial to absorb more light and increase reaction sites.

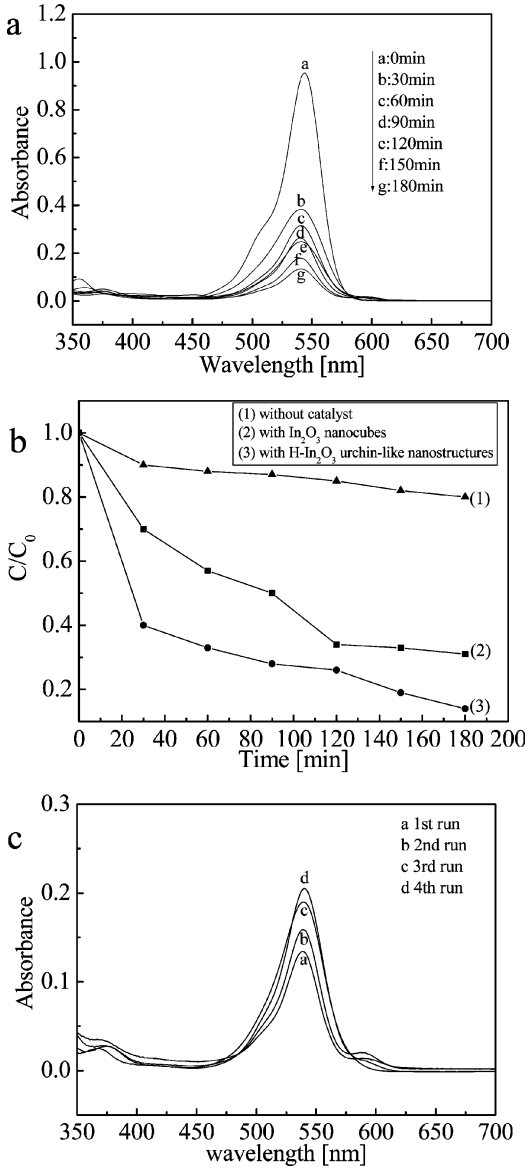

Figure 6. (a) Absorption spectra of the RhB solution (5.0×10^{-5} M, 100 mL) in the presence of H-In_2O_3 urchin-like nanostructures (25 mg) under UV light irradiation for different lengths of time. (b) Photocatalytic efficiency comparison under different conditions: (1) without any catalyst, (2) with In_2O_3 nanocubes (25 mg), and (3) with H-In_2O_3 urchin-like nanostructures (25 mg) under UV light irradiation. (c) Absorption spectra of the RhB solution under cycling runs tests of H-In_2O_3 urchin-like nanostructures with an irradiation time of 3 h.

The stability of the photocatalytic efficiency of the H-In_2O_3 urchin-like nanostructures was investigated by reuse of the photocatalysts in the fresh solution of RhB with an irradiation time of 3 h for each cycle (Figure 6c). From the UV/Vis adsorption spectra of RhB, the photocatalytic efficiency of the urchin-like nanostructured H-In_2O_3 decreases from 86 to 79% after four recycles, and the photocatalytic activity of H-In_2O_3 does not exhibit significant loss for the photodegradation of RhB. This indicates that the H-In_2O_3 urchin-like nanostructures have relatively high stability during the photocatalysis of pollutant molecules, which is important for its application. Additionally, the urchin-like structures are still retained after four recycles, indicating that the urchin-like structures are mechanically stable and can easily be separated from treated solution after photocatalysis, which is another advantage for application.

Conclusion

In summary, InOOH with urchin-like nanostructures was synthesized by a PEG-1000-assisted hydrolysis of the In^{3+} cation in water/ethanol mixed solvent. Through analysis of the various reaction parameters on the fabrication process of InOOH, we found that PEG-1000 and reaction temperature play two crucial roles in the formation of InOOH urchin-like structures. Metastable H-In_2O_3 urchin-like nanostructures were successfully prepared in high yield by annealing the InOOH precursor at 500 °C under ambient

pressure. The as-obtained H-In_2O_3 urchin-like nanostructures exhibited effective photocatalysis under UV light irradiation, which can be attributed to oxygen vacancy defects on the surface of H-In_2O_3 nanomaterials, special morphology, and the highly specific area. Additionally, H-In_2O_3 with urchin-like nanostructures has relatively high stability during the photocatalysis of pollutant molecules, which is especially important for its application.

Experimental Section

All the reagents were purchased from Shanghai Chemical Company and used without further purification.

Preparation of the InOOH Precursor: In a typical procedure, a 50-mL autoclave with a Teflon liner was charged with $InCl_3 \cdot 4H_2O$ (0.15 g, ≈0.5 mmol) dissolved in distilled water (1 mL). Then, ethanol (40 mL), urea (0.6 g, 10 mmol), and PEG-1000 (1.0 g) were added into the autoclave in turn. After the reactive mixture was stirred vigorously for 0.5 h, the autoclave was sealed and maintained at 140 °C for 16 h in a digital temperature controlled oven. The autoclave was cooled down to room temperature naturally, and the white sample was collected and washed several times with ethanol, acetone, and distilled water to remove the possible residual ions and polymer in the sample. The products were dried in a vacuum at 50 °C for 4 h. The as-prepared samples were divided into two parts. One was subjected directly to characterization and the other was submitted to the following thermal treatment.

Synthesis of H-In_2O_3: The presynthesized white sample was loaded in a quartz boat and annealed in a tube furnace at 500 °C for 5 min under ambient pressure and then cooled down to room temperature naturally. The heat rate for the tube furnace was 10 °C min^{-1} before the furnace temperature reached 500 °C. The final product, pale-yellow H-In_2O_3, was collected for subsequent characterization.

Characterization: X-ray diffraction (XRD) was preformed with a Philips X′Pert SUPER powder X-ray diffractometer with Cu-K_α radiation (λ = 1.5418 Å). Transmission electron microscopy (TEM) images were taken with a Hitachi model H-800 transmission electron microscope with tungsten filament by using an acceleration voltage of 200 kV. High-resolution transmission electron microscopy (HRTEM) images and electron diffraction (ED) patterns were obtained with a JEOL 2010 high-resolution transmission electron microscope performing at 200 kV. The field emission scanning electron microscopy (FESEM) images were taken with a JSM-6700F field emission scanning electron microanalyzer (JEOL). X-ray photoelectron spectroscopy (XPS) was operated with an ESCA-lab MKII X-ray photoelectron spectrometer. The Fourier transform infrared (FTIR) spectra of the samples were measured with a PerkinElmer FTIR spectrophotometer at room temperature. Thermogravimetry (TG) and differential thermal analysis (DTA) measure were performed with a Shimadzu TA-50WS analyzer within the temperature range from room temperature to 600 °C in air.

Photocatalytic Activity Testing: A common method for evaluating the photocatalytic activity of H-In_2O_3 urchin-like nanostructures was to examine the bleaching of RhB following UV illumination by using UV/Vis spectroscopy. In a typical procedure, the as-synthesized H-In_2O_3 urchin-like nanostructures (25 mg) used as catalyst was dispersed in absolute ethanol (99 mL). Then, RhB ethanol solution (1×10^{-3} M, 1.0 mL) was added into the H-In_2O_3 suspensions in a 200-mL conical flask. The final concentration of RhB was 1.0×10^{-5} M. A high-pressure mercury lamp with the wavelength concentrated at 254 nm was placed 20 cm away from the flask, and a sample of the irradiated mixed solution was collected every 30 min to analyze the RhB degradation by UV/Vis spectroscopy (Shimadzu DUV-3700 spectrophotometer).

Supporting Information (see footnote on the first page of this article): XPS survey spectra of as-prepared H-In_2O_3, In, and O binding energy; TGA and DTA curves of the obtained InOOH with 3D urchin-like nanostructures; FTIR spectra of PEG-1000 and precipitates.

Acknowledgments

Financial support from the National Nature Science Research Foundation of China is gratefully acknowledged.

[1] a) H. T. Ng, J. Li, M. K. Smith, P. Nguyen, A. Cassell, J. Han, M. Meyyappan, *Science* **2003**, *300*, 1249–1249; b) A. C. Chen, X. S. Peng, K. Koczkur, B. Miller, *Chem. Commun.* **2004**, *17*, 964–1965.

[2] a) C. G. Granqvist, *Appl. Phys.* **1993**, *57*, 19–24; b) H. J. Zhou, W. P. Cai, L. D. Zhang, *Appl. Phys. Lett.* **1999**, *75*, 495–497; c) A. Gurlo, M. Ivanovskaya, N. Barsan, M. Schweizer-Berberich, U. Wermar, W. Gopel, A. Dieguez, *Sens. Actuators B* **1997**, *44*, 327–333; d) S. K. Poznyak, A. N. Golubev, A. I. Kulak, *Surf. Sci.* **2000**, *454–456*, 396–401.

[3] a) Q. Liu, W. Lu, A. Ma, J. Tang, J. Lin, J. Fang, *J. Am. Chem. Soc.* **2005**, *127*, 5276–5277; b) W. S. Seo, H. H. Jo, K. Lee, J. T. Park, *Adv. Mater.* **2003**, *15*, 795–797; c) C. Li, D. H. Zhang, S. Han, X. L. Liu, T. Tang, C. Zhou, *Adv. Mater.* **2003**, *15*, 143–146; d) M. Zheng, L. Zhang, G. Li, X. Zhang, X. Wang, *Appl. Phys. Lett.* **2001**, *79*, 839–841; e) Z. Pan, Z. Dai, Z. Wang, *Science* **2001**, *291*, 1947–1949; f) J. Lao, J. Huang, D. Wang, Z. Ren, *Adv. Mater.* **2004**, *16*, 65–69; g) P. Guha, S. Kar, S. Chaudhuria, *Appl. Phys. Lett.* **2004**, *85*, 3851–3853; h) D. Chu, Y.-P. Zeng, D. Jiang, J. Xu, *Nanotechnology* **2007**, *18*, 435605–435610; i) J. Yang, C. Lin, Z. Wang, J. Lin, *Inorg. Chem.* **2006**, *45*, 8973–8979; j) A. Narayanaswarmy, H. Xu, N. Pradhan, M. Kim, X. Peng, *J. Am. Chem. Soc.* **2006**, *128*, 10310–10319.

[4] L. Brus, *Science* **1997**, *276*, 373–374.

[5] a) Z. Zhuang, Q. Peng, J. Liu, X. Wang, Y. Li, *Inorg. Chem.* **2007**, *46*, 5179–5187; b) M. Epifani, P. Siciliano, A. Gurlo, N. Barasan, U. Weimar, *J. Am. Chem. Soc.* **2004**, *126*, 4078–4079; c) C. H. Lee, M. Kim, T. Kim, A. Kim, J. Paek, J. W. Lee, S.-Y. Choi, K. Kim, J.-B. Park, K. Lee, *J. Am. Chem. Soc.* **2006**, *128*, 9326–9327; d) J. Q. Xu, Y. P. Chen, Q. Y. Pan, Q. Xiang, Z. X. Cheng, X. W. Dong, *Nanotechnology* **2007**, *18*, 115615–115921; e) C. Chen, D. Chen, X. Jiao, C. Wang, *Chem. Commun.* **2006**, 4632–4634; f) D. Yu, S.-H. Yu, S. Zhang, J. Zuo, D. Wang, Y. Qian, *Adv. Funct. Mater.* **2003**, *13*, 497–501.

[6] a) Z. P. Zhang, X. Q. Shao, H. D. Yu, Y. B. Wang, M. Y. Han, *Chem. Mater.* **2005**, *17*, 332–336; b) B. Y. Zong, Y. H. Wu, G. C. Han, B. J. Yang, P. Luo, L. Wang, J. J. Qiu, K. B. Li, *Chem. Mater.* **2005**, *17*, 1515–1520; c) B. Liu, H. C. Zeng, *J. Am. Chem. Soc.* **2004**, *126*, 8124–8125; d) B. Liu, H. C. Zeng, *J. Am. Chem. Soc.* **2004**, *126*, 16744–16746.

[7] a) M. R. Hoffmann, S. T. Matin, W. Choi, D. W. Bahnemann, *Chem. Rev.* **1995**, *95*, 69–96; b) A. Linsebigler, G. Lu, J. T. Yates, *Chem. Rev.* **1995**, *95*, 735–758.

[8] a) D. Shchukin, S. Poznyak, A. Kulak, P. Pichat, *J. Photochem. Photobiol. A: Chem.* **2004**, *162*, 423–430; b) S. K. Poznyak, D. V. Talapin, A. I. Kulak, *J. Phys. Chem. B* **2001**, *105*, 4816–4823; c) D. G. Shchukin, R. A. Caruso, *Chem. Mater.* **2004**, *16*, 2287–2292; d) S. K. Poznyak, A. N. Golubev, A. I. Kulak, *Surf.*

Sci. **2000**, *454–456*, 396–401; e) B. Li, Y. Xie, M. Jing, G. Rong, Y. Tang, G. Zhang, *Langmuir* **2006**, *22*, 9380–9385.
[9] J. C. C. Fan, J. B. Goodenough, *J. Appl. Phys.* **1977**, *48*, 3524–3531.
[10] A. Pashutski, A. Hoffman, M. Folkman, *Surf. Sci.* **1989**, *208*, L91–L93.
[11] Q. Peng, Y. Dong, Y. Li, *Angew. Chem. Int. Ed.* **2003**, *42*, 3027–3030.
[12] H. Zhang, Q. Zhu, Y. Zhang, Y. Wang, L. Zhao, B. Yu, *Adv. Funct. Mater.* **2007**, *17*, 2766–2771.
[13] a) Y. Jun, Y. Jung, J. Cheon, *J. Am. Chem. Soc.* **2002**, *124*, 615–619; b) S.-M. Lee, Y. Jun, S.-N. Cho, J. Cheon, *J. Am. Chem. Soc.* **2002**, *124*, 11244–11245.
[14] A. Kudo, K. Omori, H. Kato, *J. Am. Chem. Soc.* **1999**, *121*, 11459–11467.
[15] Y. Zheng, C. Chen, Y. Zhan, X. Lin, Q. Zheng, K. Wei, J. Zhu, *J. Phys. Chem. C* **2008**, *112*, 10773–10777.
[16] L.-Y. Chen, Y.-G. Zhang, W.-Z. Wang, Z.-D. Zhang, *Eur. J. Inorg. Chem.* **2008**, 1445–1451.
[17] F. Lu, W. Cai, Y. Zhang, *Adv. Funct. Mater.* **2008**, *18*, 1047–1056.
[18] M. Shang, W. Wang, S. Sun, L. Zhou, L. Zhang, *J. Phys. Chem. C* **2008**, *112*, 10407–10411.

Received: September 28, 2008
Published Online: January 28, 2009

